A&A, 708, A20 (2026)
https://doi.org/10.1051/0004-6361/202555807

Astronomy & Astrophysics

Quasars behind the disk of M 31 galaxy

P. Nedialkov[1,⋆], B. F. Williams[2], V. D. Ivanov[3], A. Valcheva[1], Y. Solovyeva[4], A. Vinokurov[4], E. Malygin[4], D. Oparin[4], and O. Sholukhova[4]

[1] Department of Astronomy, Faculty of Physics, Sofia University "St. Kliment Ohridski", 5 J. Bourchier blvd, Sofia 1164, Bulgaria
[2] Department of Astronomy, Box 351580, University of Washington, Seattle, WA 98195, USA
[3] European Southern Observatory, Karl-Schwarzschild-Str. 2, 85748 Garching bei München, Germany
[4] Special Astrophysical Observatory, Nizhny Arkhyz 369167, Russia

Received 4 June 2025 / Accepted 16 February 2026

ABSTRACT

Aims. Our aim is to increase the limited number of quasars behind M 31, necessary for probing the chemical content of the gas and for proper motion reference, with reliable and homogeneous redshift measurements from emission lines.

Methods. We carried out spectroscopic follow-up of 32 quasar candidates.

Results. We confirm 23 quasars. Two are new discoveries (J004029.727+403705.68 and J004215.489+412031.52) and the rest have been reported elsewhere, but with somewhat deficient analysis; 16 spectra are published for the first time. We report new homogeneous redshifts for 34 quasars (from 40 spectra, adding 17 from the archives) and summarize all available information about bona fide quasars with reliable redshift, bringing their number to 124 within the $\mu_B = 26^m/\square''$ isophote. We carried out a comparison of redshifts from different sources and excluded some objects with redshifts derived from low-resolution spectra. We derived the reddening for them from the color excess with respect to dereddened counterparts with similar redshifts in the field. Comparisons of our reddenings with M 31 reddening maps found no significant correlations.

Conclusions. Most QSOs behind M 31 show low reddening and do not probe high extinctions, probably due to a bias toward following up brighter and less extinct candidates, which underlines the need to identify fainter quasars behind nearby galaxies, especially behind higher extinction regions. Finally, the redshifts derived from low-resolution spectra must be treated with caution because they can contain significant errors.

Key words. techniques: spectroscopic – galaxies: distances and redshifts – galaxies: ISM – Local Group – quasars: emission lines – quasars: general

1. Introduction

Quasars behind nearby galaxies are of great value for probing their kinematics and interstellar medium. They establish a nonmoving reference system for astrometric studies (Kallivayalil et al. 2006; Kallivayalil et al. 2013; van der Marel et al. 2019). The quasars are background sources that allow the extinction to be studied in the intervening absorbers, which can be either nearby low-redshift galaxies or distant high-redshift objects (Crampton et al. 1997; York et al. 2006; Meusinger et al. 2010). The imprinted narrow absorption features from the interstellar material (ISM) on the quasar spectra can be used to measure the chemical composition and the velocity field of the ISM (e.g., Srianand et al. 2013; Fox et al. 2013; Richter et al. 2013; Fox et al. 2014; Combes et al. 2021). These observations, carried out in the UV, where the strong absorption features of the cold interstellar gas are, allow us to trace the chemical enrichment history of the intervening galaxies, and to trace the origin of the extended gaseous structures, such as the Magellanic stream, to a particular galaxy, in this case to the Small Magellanic Cloud. UV bright quasars are necessary for such studies, and they are usually found from surveys in the region such as GALEX (e.g., Worseck & Prochaska 2011), but they are relatively rare and only a few exist behind the nearest galaxies.

The mere identification of quasars is a challenge on its own. Usually, it is based on their optical colors (Peters et al. 2015), variability properties (Giveon et al. 1999; Chen et al. 2020), or their X-ray, UV, or mid-infrared (mid-IR) emission (Chartas et al. 2013; Morishita 2021; Guo et al. 2018, among others). The presence of a galaxy in front of the quasar introduces additional complications: contamination from foreground sources that in the general case can be variable (e.g., seeing dependent or due to the intrinsic variability of the contaminating source). However, these problems are solvable, for example, with a combination of some of these methods: Cioni et al. (2013) and Ivanov et al. (2016, 2024) easily reached a success rate of >70% despite the contamination from the Magellanic Clouds, selecting quasar candidates from near-infrared (near-IR) colors and variability. They defined a locus of previously known quasars on the $J-K_S$ versus $Y-J$ color–color diagram with photometry from the VISTA Magellanic Survey (VMC; Cioni et al. 2011), and spectroscopically followed up objects located inside this region. Its borders were adjusted to reduce the contamination, mostly from evolved stars. This is acceptable as long as the goal of the search is to efficiently identify quasars, but not necessarily to obtain a complete sample. Next, they took advantage of the time series data from the VMC survey to identify the most variable objects by parameterizing the light curves with a simple linear fit and requiring a minimum absolute slope value. M 31 and M 33 present a greater challenge than the Magellanic system due to the

---

[⋆] Corresponding author: `japet@phys.uni-sofia.bg` higher surface stellar density and the greater contamination by objects in the more crowded intervening galaxies, and because of the generally higher extinction, except for the inner SMC region.

In this paper, we report the confirmation of 23 quasar candidates behind the M 31 disk with spectra (resolution $700 \leq \lambda/\Delta\lambda \leq 1100$). Two of them are completely new discoveries, and the other 21 spectra confirm the quasar nature of previously announced candidates. We also uniformly measured redshifts for 34 unique quasars from 40 spectra, thus adding 17 archival spectra to our data. Summarizing, we built a list of 125 spectroscopically confirmed QSOs within the $\mu_B = 26^m/\square''$ isophote (Sect. 2).

The next two sections describe our target selection and the observations. Section 4 presents the analysis of the spectra, Sect. 5 is an extinction study, and Sect. 6 gives a summary.

2. Target selection

M 31 and M 33 present a greater challenge than the Magellanic Clouds, due to the higher surface stellar density. The census of the quasars behind any galactic disk depends on its adopted boundaries. For example, Massey et al. (2019) list eight previously known and seven newly found QSOs[1] within the footprint of M 31 Local Group Galaxy Survey (LGSS; Massey et al. 2016). Three more QSOs that were known at the time were missing in this list: one reported by Huo et al. (2013) and two others reported by Liao et al. (2019), bringing the total number of known QSOs within this survey to 18.

However, the LGSS was designed to cover the region of active star formation, especially the eastern side that is farther from the Milky Way; the M 31 disk extends farther outside the survey's footprint. To compensate for this offset, we adopt here a wider and physically defined area of interest adopting as a galaxy limit the ellipse with a major diameter D26 = 225′, corresponding to the surface brightness level $\mu_B = 26^m/\square''$ of Walterbos & Kennicutt (1987). We adopt a position angle PA=35 deg and a major-to-minor diameter ratio of 3.09 that RC3 (Third Reference Catalog of Bright Galaxies; de Vaucouleurs et al. 1991) reports for the somewhat brighter, but better defined standard isophote of μ_B=$25^m/\square''$. For the center of M 31, we adopt the coordinates as determined in 2MASS (Skrutskie et al. 2006): α=0:42:44.33 δ=+41:16:07.5 (J2000). Our ellipse encompasses well all the footprints of the modern catalogs with IR and optical photometry in M 31, as well as the dust maps available in the literature.

We found spectra of six candidates, in addition to the 18 previously known quasars within the selected area. Four of these extra spectra were observed by the Large Sky Area Multi-Object Fibre Spectroscopic Telescope (LAMOST) as a part of its Quasar Survey 2012–2017 (Dong et al. 2018; Liao et al. 2019) and are publicly available in LAMOST DR5[2]. Two other QSOs are reported by Huo et al. (2013). Interestingly, the latest LAMOST Quasar Survey DR6–DR9 2017–2021 (Jin et al. 2023) does not report any QSOs behind the M 31 disk.

In total, there are 25 objects with spectroscopically derived optical redshifts within the D26 ellipse: 24 bona fide QSOs with prominent emission lines and a BL Lac discovered by Paiano et al. (2017). Their positions are shown in Fig. 1, together with the D26 and D25 isophotes and the footprints of M 31 photometric catalogs: Massey et al. (2016), Williams et al. (PHAT; 2014) and Khan (*Spitzer* PSC; 2017).

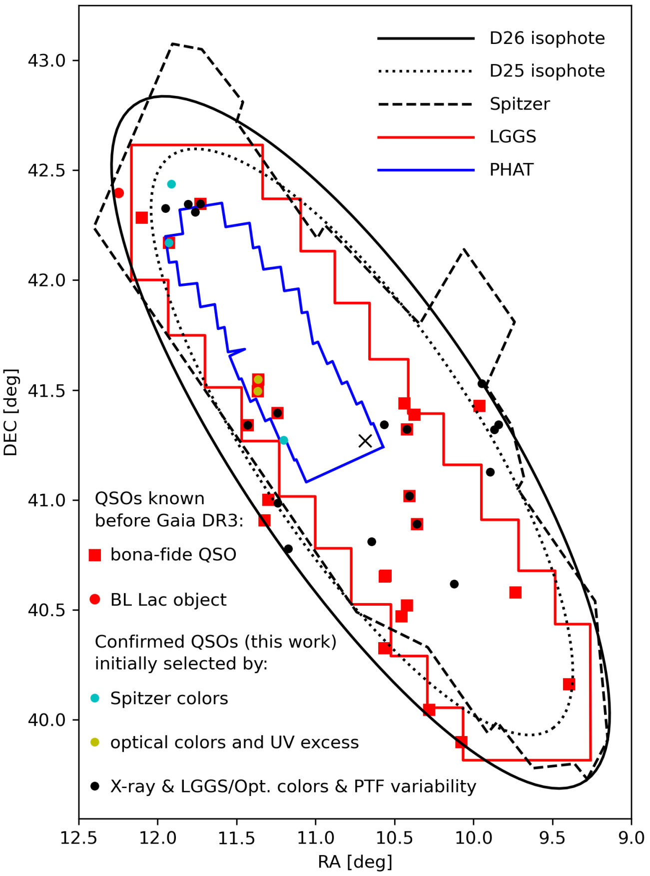

Fig. 1. Map of the 24 bona fide QSOs (red squares) with prominent emission lines and 1 BL Lac object (red dot) known from the literature before *Gaia* DR3 (Gaia Collaboration 2023b). The confirmed QSOs from our target list are also shown: 3 *Spitzer*-selected (cyan), 2 selected from optical colors and UV excess (yellow), and 18 selected by other means (see Table A.1; black). All objects are located within the $\mu_B = 26^m/\square''$ isophote (black solid line). The μ_B=$25^m/\square''$ isophote (dotted line), the approximate boundaries of the *Spitzer* PSC catalog (dashed line) and the footprints of LGGS (red) and PHAT (blue) catalogs are also plotted.

Recently, *Gaia* DR3 contributed to the global census of QSOs adding 6.4 million sources classified as active galactic nuclei (AGN) (Delchambre et al. 2023). The extragalactic catalog of *Gaia* DR3 (Gaia Collaboration 2023b) reports parameters derived from various post-processing modules dedicated to the classification and characterization of more than 6.64 million objects considered as QSO candidates, but only 159 quasar candidates behind the M 31 disk are classified as AGN. Among them 120 have derived redshifts based on the spacecraft's spectrograph with a resolving power R ∼ 30–100. However, a careful comparison with better quality data from the literature, including our own measurements reported here, suggested that about 30% of these redshifts are significantly different from measurements that we deem more reliable. This broadly agrees with their own assessment that ∼36% of the quasars have redshift

---

[1] Here, we use quasar, QSO, and AGN interchangeably because determining the exact energetics of each object is beyond the scope of this work. Furthermore, the observed broad emission lines indicate that our sample is dominated by Type 1 QSOs.

[2] `http://dr5.lamost.org/v3/sas/fits/`

errors >0.1 dex, and in the Quaia survey[3] there is an even higher fraction of ~47% (if the warning flags are ignored). Therefore, we omitted from our analysis these *Gaia* redshifts. Objects included in this list are still considered, if other sources reported redshifts and those other redshifts were used.

Dey et al. (2023) listed 184 quasars behind the disk of M 31 from spectroscopy with Dark Energy Spectroscopic Instrument (DESI; DESI Collaboration 2024), but only 14 of them are located within D26 ellipse. They are by-products of a comprehensive spectral survey (resolution $2000 \leq \lambda/\Delta\lambda \leq 5500$) of 11 416 objects on the Mayall 4m telescope at KPNO in two fields with $3\overset{\circ}{.}2$ diameter, one centered on M 31 itself and the other to the south of it. The selection criteria involve negligible parallaxes and proper motions and combine *Gaia* DR2 and unWise photometry (Lang 2014; Schlafly et al. 2019). They do not list errors, but 51 of their quasars – many located far outside the disk of M 31 – have redshifts in Barkhouse & Hall (2001), Neugent et al. (2012), Huo et al. (2013), Dong et al. (2018), Massey et al. (2019), and Liao et al. (2019). Their object No. 141 with z=1.778 is classified based on the LAMOST spectrum as a star at the velocity of M 31, and for their object No. 39 the LAMOST redshift is 1.600, as opposed to their 2.956; for the remaining objects the mean redshift difference is 0.004±0.016. We consider this a reliable source of confirmed quasars.

Storey-Fisher et al. (2024) revisited the *Gaia* spectra, also combining them with unWISE colors. They implemented cuts based on proper motions and colors, thereby reducing the number of contaminants by approximately fourfold. They used machine learning to improve the *Gaia* redshift estimates. Based on the same low-resolution *Gaia* spectra, the number of catastrophic outliers was reduced by a factor of 3 with respect to the unvetted analysis; however, 91% of their redshifts agree with the SDSS DR16 measurements (Lyke et al 2020) to within 0.2 dex. The final catalog contains 1 295 502 quasars with G<20.5 mag, and 755 850 candidate objects in an even cleaner G<20.0 mag sample. They reported 105 QSOs within the M 31 disk. There are 54 counterparts in *Gaia* DR3 that have a Class AGN, and the remaining 50 are not classified.

Our data and the literature reports produce a sample of 124 unique bona fide spectroscopically confirmed quasars and 1 BL Lac within the $\mu_B = 26^m/\square''$ isophote. The sample selection is heterogeneous because of the non-uniform coverage of different surveys that provided the photometric data. Therefore, it is difficult to estimate the selection bias and completeness of our search (see Sect. 4.2).

Thirteen spectra came from a campaign to confirm optical and X-ray selected high-mass binaries in M 31 (Williams et al. 2014); 12 of them were identified as quasars and 1 was an M star (No. 14 in Table A.1). Next, we expanded our search to the mid-IR. Initially, its footprint was limited to the Panchromatic Hubble Andromeda Treasury survey (PHAT; Williams et al. 2014) where deep and high angular resolution imaging allowed isolated bright candidates to be identified that meet the mid-IR criteria of Mateos et al. (2012), based on colors from the Wide-field Infrared Survey Explorer (WISE; Wright et al. 2010). This is shown in Fig. 2 (top panel). We obtained spectra of four candidates from this selection.

We further expanded the target selection to include the Local Group Galaxy survey (LGGS; Massey et al. 2016) combining it with mid-IR *Spitzer* photometry of Khan (2017). Following Mateos et al. (2012), we defined a locus (Fig. 2, middle) of known quasars in the *Spitzer* colors space as follows:

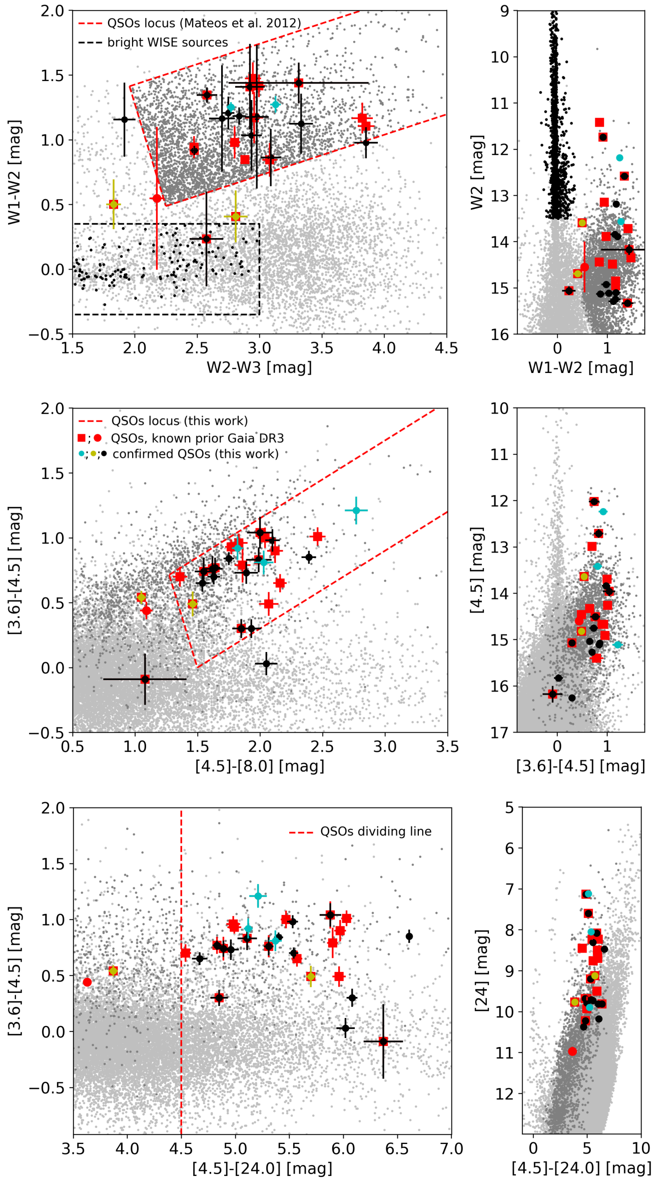

Fig. 2. Illustration of our MIR color selection (see Sect. 2 for details). Top: WISE color–color diagram (left) and color–magnitude diagram (right). The symbols in all panels are the same as in Fig. 1. The small gray dots show the entire WISE photometry within the *Spitzer* footprint. The small black dots are the sample of bright WISE sources used to adjust the coordinates (see Appendix E for details). The red dashed lines show our adopted quasar locus defined in Eq. (1) after Mateos et al. (2012). The sources falling inside are plotted in dark gray in all panels. Middle and bottom: Similar diagrams, but respectively with *Spitzer* 3.6, 4.6 μm and 8, 24 μm bands. The dashed vertical line in the bottom plot shows our additional color constraint. Summarizing, our targets for follow-up spectroscopy were selected from among the dark gray points that meet this additional criterion.

$$\begin{aligned}
&([3.6]-[4.5]) \geq -3.17 \times ([4.5]-[8.0]) + 4.75;\\
&([3.6]-[4.5]) \geq 0.6 \times ([4.5]-[8.0]) - 0.90; \qquad (1)\\
&([3.6]-[4.5]) \leq 0.6 \times ([4.5]-[8.0]) - 0.05.
\end{aligned}$$

This is an intentionally conservative definition that excludes some known quasars, but it helps to reduce the contamination

---

[3] https://zenodo.org/records/10403370

by red stars. In addition, we required that ([4.5]−[24])≥4.5 mag and that the sources are isolated; the degree of crowding index defined by Massey et al. (2016) is <5%. Nineteen (∼85%) of the 22 known quasars fall within the locus defined by these criteria; the three remaining sources are nearby AGN where the nuclei may be contaminated by the emission from the galaxy disks (Fig. 2, bottom). Even these conservative criteria yielded hundreds of potential QSOs, but only a handful of them were bright enough in the optical for follow-up spectroscopy: 10 have R≤19.2 mag, 32 have 19.2<R≤20.0 mag, and 62 have 20.0<R≤20.5 mag, giving us in total 104 LGGS objects within a searching radius of 1.5″. We obtained spectra of only eight of these.

Seven quasars from Yuhan Yao[4] were reidentified among known X-ray sources (Flesch 2015) and were reobserved producing homogeneous redshifts for six of them. The remaining object (No. 4 in Table A.1) was classified as an X-ray binary.

The complete list of 32 observed candidates is given in Table A.1. In the process of matching the optical and mid-IR surveys, we discovered some systematic differences in the coordinates of Khan (2017). The applied corrections with respect to the WISE catalog are described in Appendix E.

3. Observations and data reduction

The spectroscopic confirmation was obtained by low-resolution optical spectroscopy, which allows quasars to be recognized from the broad emission lines in their spectra. Part of the spectra were obtained with the Dual Imaging Spectrograph[5] (DIS) at the 3.5m telescope at the Apache Point Observatory (labeled A in the Tel. column in Table A.1), with the B400 and R300 gratings in the blue (λ≈3425–5900 Å) and red (λ≈5180–9860 Å) channel, respectively. The 1.5 arcsec slit was used, delivering a resolving power of R≈700 and 850 at the centers of the wavelength ranges for the blue and red arms, respectively.

The remaining spectra were obtained at the 6m telescope at the Special Astrophysical Observatory (SAO) of the Russian Academy of Sciences (labeled B in the Tel. column in Table tab:obslog) with SCORPIO-1[6] (grisms VPHG1200B and VPHG1200R, spectral ranges and resolutions are λ≈3600–5400 Å and R≈800, λ≈5700–7400 Å R≈1300, respectively; 1.2 arcsec wide slit; Afanasiev & Moiseev 2005) and SCORPIO-2[7] (grism VPHG1200@540, spectral range λ≈3650–7250 Å, resolution R≈1000; 1.0 arcsec wide slit; Afanasiev & Moiseev 2011). Table A.1 shows the log of our observations.

The data were reduced with the Image Reduction and Analysis Facility[8] (IRAF; Tody 1993, 1986) and the ESO Munich Image Data Analysis System[9] (MIDAS; Banse et al. 1988; Warmels 1992). The usual steps for long-slit data processing were performed: bias and dark subtraction, flat-fielding, and wavelength calibration. The one-dimensional spectra were extracted within 0.8–1.2 arcsec wide apertures, approximately matching the seeing during the observations for the DIS data, or using the optimal extraction code SPEXTRA, specifically designed for crowded fields (Sarkisyan et al. 2017) for the SCORPIO data. The spectra were flux calibrated with spectrophotometric standards from Oke (1990) and Hamuy et al. (1992, 1994), but given the non-photometric conditions during most of the observations, it is relative, so we only recovered the correct shape of the spectra, not their absolute flux. The quasar spectra are plotted in Fig. 3.

Broadband *grizy* photometry for the quasars behind M 31 and in the surrounding field was obtained from the Pan-STARRS Survey DR1 (Chambers et al. 2016).

4. Quasar sample

The presence of broad lines in our spectra indicates that 23 (yellow, cyan, and black solid dots in Fig. 1) out of the 32 observed objects are quasars; J004029.727+403705.68 and J004215.489+412031.52 (No. 6 and 11 in Table A.1, respectively) are new and the rest are confirmations, although for 16 of these our spectra are the first to be published; the nine non-quasars are stars or galaxies, or their nature cannot be reliably identified because of the low signal-to-noise of the spectra. Among 13 X-ray selected candidates, 12 turn out to be quasars; the UV excess in LGGS-PHAT selected 4 candidates, which yielded 2 quasars; the *Spitzer*-LGGS selected 8 candidates, which also yielded 3 quasars; 6 of the 7 Yuhan Yao objects appear to be quasars. By analyzing 17 archival spectra in addition to our data, we uniformly measured redshifts for a total of 34 unique quasars based on 40 spectra in total.

The objects with measured redshift in this work together with the literature QSOs with a spectroscopically derived redshift form a sample of 125 QSOs located within the M 31 isophote $\mu_B = 26^m/\square''$. They are listed in Table B.1, together with the lines used for the redshift measurements and the distances from the M 31 center. For the center of M 31, we adopted the coordinates of its extended core J004244.33+411607.5 (Skrutskie et al. 2006) located at 1.7″ from the center defined in RC3 (de Vaucouleurs et al. 1991). All distances ρ within the rectified plane of the galaxy are in fractions, normalized to ρ_{25}, which is one-half of the major isophotal diameter D25=190.5′ measured at surface brightness level μ_B=$25^m/\square''$. They are calculated assuming position angle PA=35 deg, and determined as the ratio of the major to minor isophotal diameters R25=3.0903 (de Vaucouleurs et al. 1991) and taking into account an intrinsic oblateness of 0.14, typical for a Sb galaxy such as M 31. Thus, the disk plane is inclined to the line of sight at 17.1 deg.

To outline the area of interest in this work, we tentatively adopted a larger major isophotal diameter of 225′ as measured approximately at surface brightness level $\mu_B = 26^m/\square''$ by Walterbos & Kennicutt (1987), and the same axis ratio and PA as in RC3. We note that the Holmberg diameter of 200′ (Nilson 1973) falls just between the previous two values, but the axis ratio of 2.5 leads to a smaller inclination of 12.1 deg.

4.1. Redshift measurements

Quasars are easy to identify from the broad lines (as wide as thousands of km s^{-1}), for example C IV 1548, C III] 1909, Mg II 2799, and others, emitted by the gas in the vicinity of the central supermassive black holes (BH; Bahcall et al. 1997; Peterson 1997). We measured their redshifts closely following the procedures of Ivanov et al. (2016) and Massey et al. (2019). First, we

---

[4] `https://speakerdeck.com/yaoyuhan/quasars-behind-m31-from-ptf-survey`

[5] `https://www.apo.nmsu.edu/arc35m/Instruments/DIS/`

[6] `https://www.sao.ru/hq/lsfvo/devices/scorpio/scorpio.html`

[7] `https://www.sao.ru/hq/lsfvo/devices/scorpio-2/index.html`

[8] IRAF is distributed by the National Optical Astronomy Observatory, which is operated by the Association of Universities for Research in Astronomy under a cooperative agreement with the National Science Foundation.

[9] `https://www.eso.org/sci/software/esomidas/`

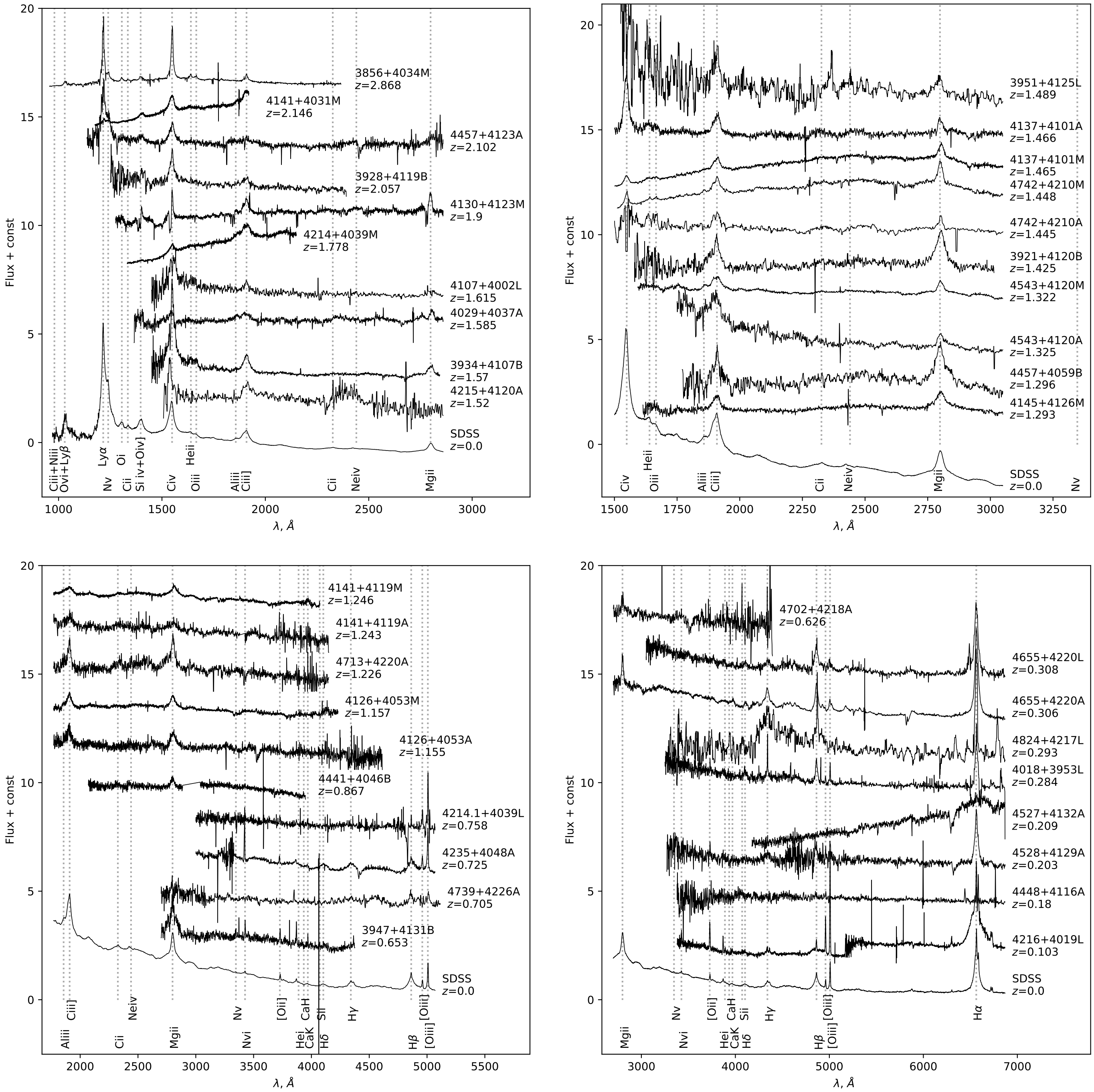

Fig. 3. Spectra of the observed objects sorted by redshift, shown at rest-frame wavelength. Some more prominent features are marked with vertical dashed lines and are labeled. The SDSS composite quasar spectrum (Vanden Berk et al. 2001) is also plotted at the bottom of each panel.

identified the broad lines comparing the spectrum of each object with the composite SDSS quasar spectrum of Vanden Berk et al. (2001). Then, we measured the observed wavelengths of the lines fitting Gaussians to them with the IRAF task splot and calculated the redshift of each line. Blended lines were omitted. Lines affected by strong intervening absorption were omitted or, if possible, Gaussians were fitted only to their cores. The final redshift of an object was determined by averaging the redshifts of all emission lines. The redshift uncertainty was the r.m.s. of the redshifts of the individual lines; if only two lines were available, we tentatively adopted as an error the difference between their redshifts.

4.2. Comparison with literature redshifts

In general, our redshift measurements z_4, shown with dots in Fig. 4 (right), agree well with the literature with a few exceptions. For example, we measured z=0.626±0.011 for Gaia DR3 375328395906539392 (Nos. 28 in Table A.1 and 109 in Table B.1), while Gaia Collaboration (2023a) and Storey-Fisher et al. (2024) reported the vastly different z=2.419±0.016 and z=1.088±0.188, respectively. We identified the single emission line in its spectrum as MgII 2799 because no other prominent lines appeared within the wavelength coverage of our APO spectrum, and they should have if the redshift had been different.

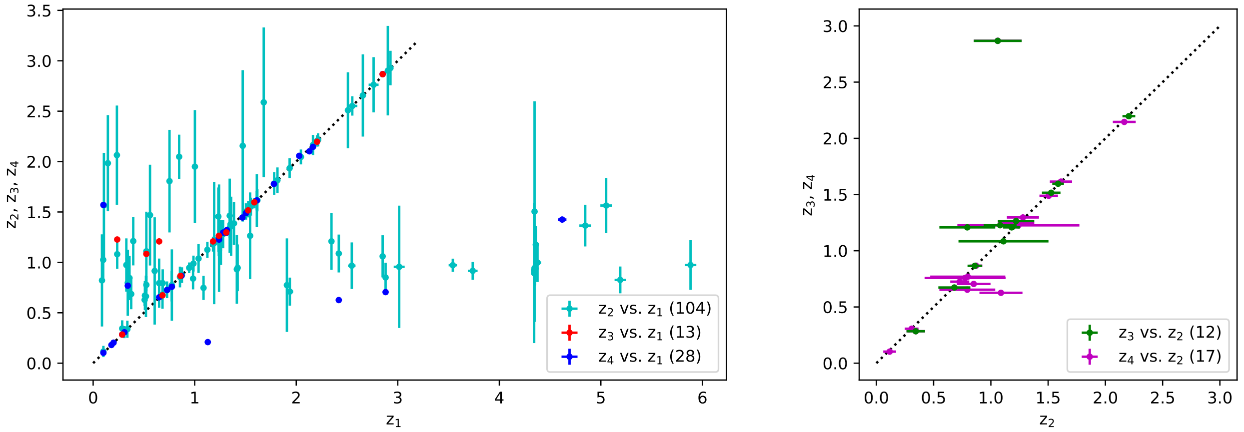

Fig. 4. Cross-comparison of redshifts from different sources: z_1 – Gaia Collaboration (2023a); z_2 – Storey-Fisher et al. (2024); z_3 – Dey et al. (2023); z_4 – all other sources (listed in Table B.1), including this work redshift preference when available. Left: z_2, z_3, and z_4 vs. z_1. Right: z_3 and z_4 vs. z_2. The published measurement errors are shown, except for Dey et al. (2023) who do not list them; in this case for plotting purposes we adopted errors equal to 0.005 dex. The bracketed numbers in the legends show how many objects constitute the overlapping subset between each pair of samples. The black dotted line has a slope of one.

For Gaia DR3 375423881617811328 (Nos. 30 in Table A.1 and 115 in Table B.1), we measured z=0.705±0.001, agreeing at ∼1σ level with z=0.850±0.147 of Storey-Fisher et al. (2024), but very different from z=2.880±0.026 of Gaia Collaboration (2023a). Our measurement is based on three lines, making the random agreement unlikely.

Gaia DR3 369288714109887744 (Nos. 23 in Table A.1 and 92 in Table B.1) is another case of disagreement. This is a rediscovered quasar at z=0.209±0.001 found earlier by Dorn-Wallenstein, Levesque, & Ruan (2017) at z ∼ 0.215. A third measurement of z=1.129±0.008 (Gaia Collaboration 2023a) is considered unreliable.

The largest redshift discrepancy is associated with Gaia DR3 381231021002898048 (Nos. 1 in Table A.1 and 15 in Table B.1). Our higher quality SAO spectrum yields 1.425±0.005, very different from the z=4.619±0.042 of Gaia Collaboration (2023a). Notably, this work gives some extremely high redshifts with respect to Storey-Fisher et al. (2024) for 21 other quasars.

For two objects, we measured redshifts higher than the values of Gaia Collaboration (2023a). For DR3 375418590218050304 (Nos. 32 in Table A.1 and 118 in Table B.1), they reported z=0.341±0.003, while we measured z=0.769±0.002, very similar to the z=0.798±0.328 of Storey-Fisher et al. (2024). The decisive argument for our higher redshift is the identification of Mg II 2799 in the blue arm of the APO spectrograph. The two arms are calibrated independently, and in effect they are two instruments.

For Gaia DR3 381223637953333376 (Nos. 3 in Table A.1 and 18 in Table B.1), we measured z=1.570±0.001. Gaia Collaboration (2023a) place it at z=0.101±0.008, which is inconsistent with our excellent quality SAO spectrum that exhibits multiple emission lines.

Not surprisingly, there is a somewhat better agreement between z_3 (Dey et al. 2023) and z_2 (Storey-Fisher et al. 2024), and between our redshifts z_3 and z_2 (Storey-Fisher et al. 2024), as seen in Fig. 4, right. The only inconsistent case here is Gaia DR3 381137287633113216 (No. 7 in Table B.1): Storey-Fisher et al. (2024) reported z=1.060±0.209, very different from our value of z=2.868±0.003. Our value agrees with three other measurements from the literature.

The blazar Gaia DR3 375378320605062144 (Paiano et al. 2017) was excluded from our redshift and reddening analyses because of the contradicting z measurements in the literature and because it may not exhibit typical quasar colors. Some objects were misidentified as quasars in the literature. Liao et al. (2019) reported that LAMOST_10.952+40.80076 (Gaia DR3 369228137893480064) is a QSO at z=0.262. However, a careful inspection of the LAMOST DR5 spectrum (spec-55859-M5901_sp04-015) revealed prominent CaT and other stellar features typical for K7-M0 stars. Another example is Gaia DR3 381200372113648128, listed as J003905.66+410456.6 in LAMOST DR2&3 (Dong et al. 2018) and LAMOST_9.774+41.08240 in LAMOST DR4 (Liao et al. 2019). We did not find convincing confirmation of the z ∼ 0.8 derived in both these papers from the LAMOST spectra. Instead, we identified a broad feature corresponding to Hα at the M 31 rest frame, and we suspected that it has been misinterpreted as C IV 1548 by Gaia Collaboration (2023a), who reported z=3.190±0.027.

Our selection identified nine more QSO candidates within the $\mu_B = 26^m/\square''$ isophote, and we observed them (Nos. 5, 7, 13–17, 19, 26 in Table A.1), but the spectra did not provide evidence for a quasar nature. This was the case with object No. 16, located in a prominent dust lane. Johnson et al. (2015) reported a probability of ∼10% that it is a galaxy. However, our spectrum lacks broad emission lines and shows absorptions making it a likely red star or a globular cluster in M 31. These nine and the two LAMOST objects mentioned above were omitted from Table B.1.

The heterogeneous nature of the selection and the lack of comparison quasars outside of the M 31 disk, confirmed by the same means and following the same strategy makes it difficult to estimate the completeness of this sample. The only exception, and the largest contribution to our sample, bringing in about two-thirds of the quasars, is the all-sky Quaia survey. We compared the surface density of secure quasars, according to the classification of Gaia Collaboration (2023a, see their Class, reproduced here in Table B.1). There is a 10–30% excess of such objects inside of the $\mu_B = 26^m/\square''$ isophote, where the exact percentage depends on the adopted outside locus and magnitude limits. Therefore, it is not the incompleteness, but rather the contamination that may be an issue for quasar searches, underlying the

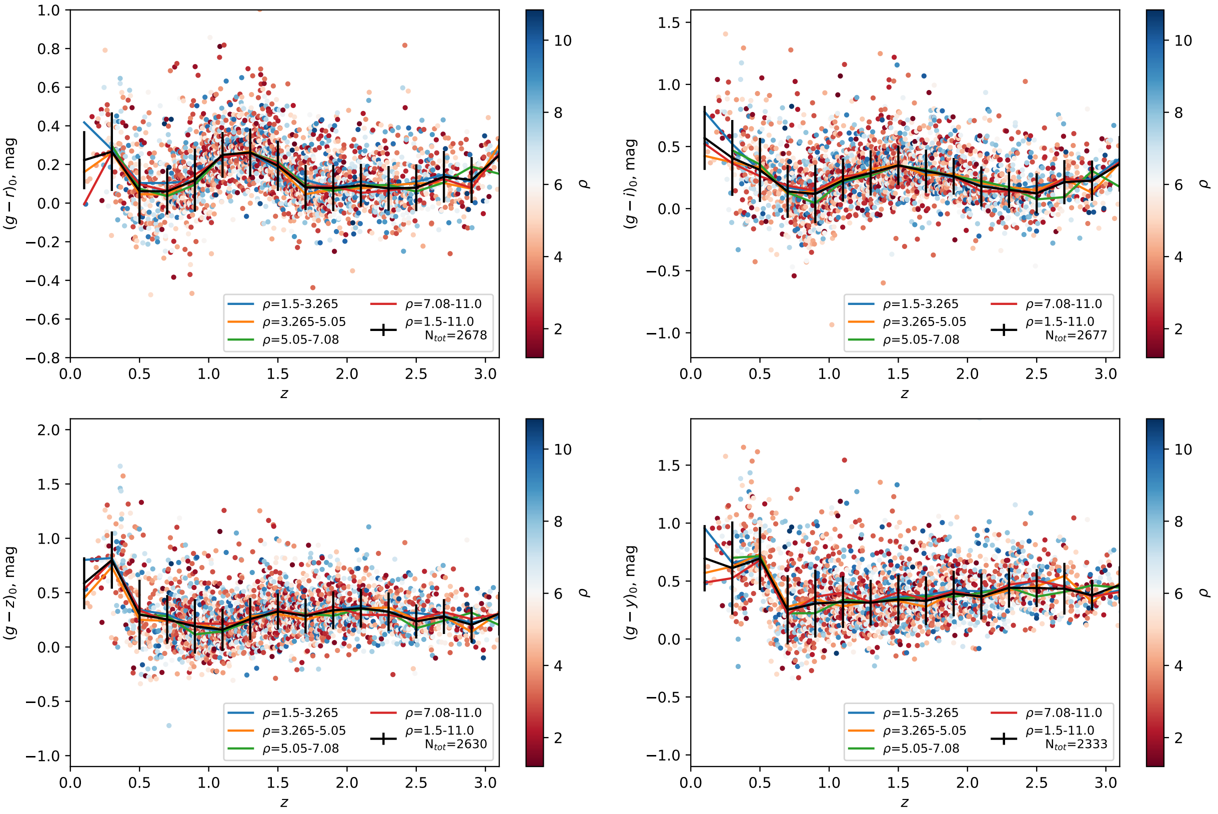

Fig. 5. Intrinsic colors of our Quaia reference quasar sample, obtained after correcting the Pan-STARRS Survey DR1 *grizy* photometry (Chambers et al. 2016) for the Milky Way extinction according to the Schlafly & Finkbeiner (2011). The color of the points marks the distance of the quasars from the M 31 center ρ in units of ρ_{25} isophotal radii. The distance between the bins was set to ensure these bins contain similar number of quasars. The solid lines connect the median colors within 0.5 dex wide redshift bins. The vertical error bars are the standard deviations of the colors of all quasars within each redshift bin, regardless of the distance from the M 31 center, and they were calculated as 1.48×MAD (median absolute deviation) to suppress the influence of outliers.

need for reliable spectroscopic confirmation, for example the follow-up we report here.

4.3. Reliability of redshift measurements

To assess the reliability of heterogeneous literature redshifts, we compared the multiple measurements that are available for some sources (Fig. 4). Gaia Collaboration (2023a) reported some relatively high redshift measurements that found no confirmation among other sources (pale blue dots in the left panel). Many outliers in Fig. 4 (left) have a probability P_{QSO} of being a quasar of ~100%, which brings into question the reliability of P_{QSO} and the values of their redshifts. Further investigation revealed that these high redshifts are associated with objects not classified as active galaxies or altogether lacking classification in Gaia Collaboration (2023a, again, refer to the Class in Table B.1). Therefore, the redshifts in *Gaia* DR3 must be treated with caution, unless the object is specifically classified as a high-probability active galaxy.

Other literature sources were in better agreement. For example, Ivanov et al. (2024) finds good agreement between their own redshifts and the Quaia measurements. However, taking the literature redshifts at face value seems risky. To ensure we use the most reliable redshifts, we adopted the following strategy: if an individual redshift measurement for an object is available (e.g., from our own spectra or from the literature), we prefer this value because as a rule they are human-verified, as opposed to redshifts from large surveys that rely as a rule on automated procedures. This is largely driven by our concern about the objects with $z>3$ of Gaia Collaboration (2023a). In total, 18 quasars fall into this group. We note that some of the spectra come from the literature, but we reidentified the emission lines and remeasured the redshifts.

If no individual measurements were available, we turned to survey data. In order of preference we used Dey et al. (2023) and Storey-Fisher et al. (2024). These two surveys contributed 9 and 81 redshifts, respectively. This brings the total number of quasars with spectroscopic redshifts within the $\mu_B = 26^m/\square''$ isophote to 124, omitting the blazar, as discussed earlier.

5. M 31 disk extinction

We attempted to measure the extinction within the M 31 disk from the color excess of quasars within the $\mu_B = 26^m/\square''$ isophote with respect to the colors of quasars at similar redshift, located away from M 31. We assumed that they show on average the same colors, as long as they are at the same redshift, and that the large number of quasars away from the disk will average out any intrinsic variations.

First, we corrected both quasar samples for the foreground Milky Way extinction. Outside of M 31, we applied individual estimates from the map of Schlafly & Finkbeiner (2011). Within the M 31 body, the predicted E$(B-V)$ increased inward, due to the dust content of the galaxy itself. To alleviate this issue, we adopted for all objects inside the $\mu_B=26^m/\square''$ isophote a constant foreground Milky Way extinction. We considered 326 Quaia quasars within an elliptical annulus between one and two major-axis D26 isophotal diameters, to ensure that they were safely clear of M 31, but still in the general direction of the galaxy, minimizing any residual Milky Way extinction. Averaging the individual extinctions, we derived E($B-V$)=0.060±0.010 mag, similar to E($B-V$)=0.055 mag that Schlafly & Finkbeiner (2011) report for the M 31 center and well within the range 0.035−0.105 mag that the same map enables.

Next, we derived the intrinsic colors $(g-r)_0$, $(g-i)_0$, $(g-z)_0$, and $(g-y)_0$ at the redshift of each quasar behind M 31, as the median over the dereddened colors of all quasars in the reference sample with redshift within 0.3 dex (Fig. 5). This reference sample was selected from the Quaia catalog to include all quasars within 5 deg from the M 31 center (about 2600 objects in total; see Fig. 5 for the exact numbers in the individual colors), but outside the $\mu_B=26^m/\square''$ isophote, to ensure averaging over 100's of quasars. We converted the color excesses to A$_V$ adopting a total-to-selective extinction ratio R$_V$=3.1 and according to the extinction law of Cardelli et al. (1989). We formed the A$_V$ error for each quasar behind M 31 as a quadrature sum of the quasars' photometric errors and the variation of the intrinsic colors for the quasars at that redshift. We averaged the derived A$_V$ values from the four colors with error weighting. Some extinctions are negative because of the large intrinsic spread of quasar colors that can be seen in Fig. 5 and to a lesser extent, the photometric errors. Furthermore, undetected contamination from blue foreground objects in M 31 itself may also lead to negative extinction, although we tried to exclude this by selecting isolated candidates for the follow-up. No trend in the evolution of the broadband intrinsic colors of quasars as a function of redshift is seen when the sample is divided into several radial bins spanning 1.5–11 ρ_{25}[10].

We used two M 31 extinction maps to compare our estimates with. The map of Draine et al. (2014) has the SPIRE 350 resolution of 25″. It gives the dust surface density and its uncertainty in units of ($M_\odot$/kpc^2). We converted these quantities into absorption A_V values according to the Draine & Li (2007) dust model. The map of Dalcanton et al. (2015) has 7″ resolution. It derives A$_V$ using the stellar photometry of the red giant branch (RGB) stars from the Williams et al. (PHAT; 2014) survey, enabling a direct comparison with our results. Only 114 of our quasars fall within the footprint of the former map and 14 of the latter. No correlation is found in either case (Fig. 6). This negative result is probably due mostly to the bias toward lower extinction that is rooted in the quasar selection and especially in the target selection for the spectroscopic confirmation: quasars located along more heavily obscured lines of sight are fainter and less likely to have spectra. This can be seen in Fig. 7 that overplots the quasars in the sample on the Draine et al. (2014) reddening map. Furthermore, with quasars we measure the extinction along a narrow line of sight, while the reddening maps average the extinction over wider bins. Last but not least, the number of quasars may be insufficient for this test, considering the significant variation of the quasar's intrinsic colors (Fig. 5).

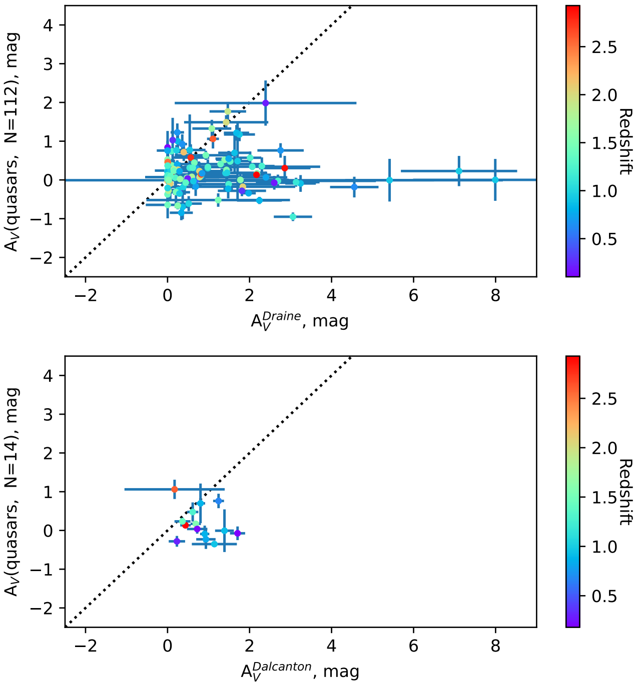

Fig. 6. Comparison of A$_V$ derived from our quasar sample and from the reddening maps of Draine et al. (2014, top) and Dalcanton et al. (2015, bottom).

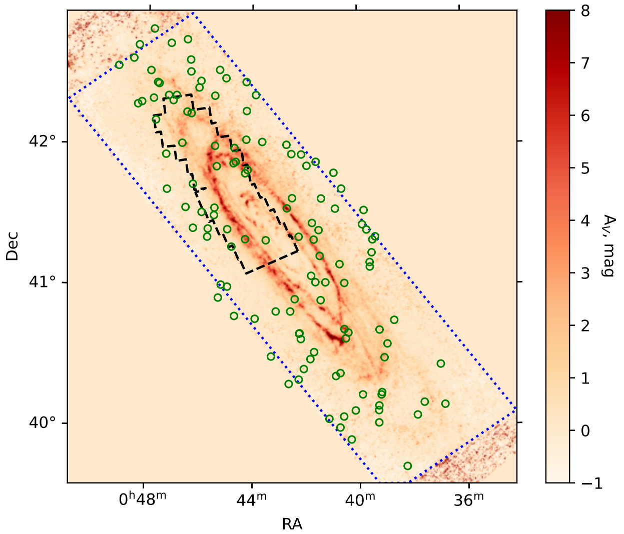

Fig. 7. Location of the quasars from our sample on the reddening maps (green open circles) of Draine et al. (2014, blue dotted line) and Dalcanton et al. (2015, black dashed line).

6. Summary and conclusions

We selected quasar candidates from the apparent colors and X-ray emission among objects within the M 31 $\mu_B=26^m/\square''$ isophote and carried out optical spectroscopy of the brightest of them to confirm their nature increasing the number of published spectra from 24 to 40. We also collected quasars from various public surveys, bringing the total number of bona fide quasars behind the M 31 disk to 124 (125 when counting one blazar).

Our work provides a large sample of quasars for astrometric studies of M 31 (i.e., Rusterucci et al. 2024), similar to the previous work in the Magellanic Clouds (Costa et al. 2011). Quasars

---

[10] A stand-alone Python script that derives the intrinsic colors of quasars as a function of redshift from a sample of references quasars outside M 31, and then calculates the color excesses and absorptions for individual quasars behind the M 31, is available at `https://github.com/vdivanov/Quasars_behind_M31_2026/`, together with the necessary input files.

also facilitate the study of its interstellar medium (ISM), of the extinction from their colors, as we attempted to do here, and of the ISM's chemical abundances with spectroscopy, typically in the UV (Fox et al. 2013; Mishra et al. 2024). The later work will come within reach for many faint quasars with the next generation of 30–40 m class spectroscopic telescopes or with the dedicated spectroscopic facilities, such as the WST (Wide-field Spectroscopic Telescope; Mainieri et al. 2024).

We measured the extinction inside M 31 toward 114 quasars with reliable redshifts and found no correlation with the existing reddening maps, probably because of the limited number of objects, the biases in our sample, and different physical scales of the regions that are probed with the quasars and the dust maps. This problem must be revisited when LSST helps to discover more quasars, based on their variability, as Ivanov et al. (2016, 2024) demonstrated that the variability helps to increase the efficiency of quasar selection.

Last but not least, in the course of our analysis we confirmed the previous concerns that the redshifts, derived from low-resolution spectra, may contain significant errors. These measurements must be treated with caution.

Data availability

The dataset (with pdf converted to a proper table), and the full Tables B.1 and C.1 are available at the CDS via `https://cdsarc.cds.unistra.fr/viz-bin/cat/J/A+A/708/A20`.

Acknowledgements. The authors thank an anonymous referee whose valuable comments and recommendations helped to improve the quality of the paper. PN and AV acknowledge financial support from the European Union-NextGenerationEU, through the National Recovery and Resilience Plan of the Republic of Bulgaria, project No. BG-RRP-2.004-0008-C01. PN thanks Phillip Massey for sharing the spectra of 10 QSOs behind the disk of M 31 obtained with Hectospec at the MMT. P.N. is also grateful to Julianne Dalcanton for providing the extinction maps of the M 31 disk, based on the PHAT survey data. The search for QSOs behind the disc of the M 31 galaxy was partially supported by a short-term scholar Fulbright grant of P.N. at the Department of Astronomy, University of Washington, for the academic year 2018– 2019 from the US Department of State program number G-1-00005. This work has made use of data from the European Space Agency (ESA) mission *Gaia* (`https://www.cosmos.esa.int/gaia`), processed by the *Gaia* Data Processing and Analysis Consortium (DPAC, `https://www.cosmos.esa.int/web/gaia/dpac/consortium`). Funding for the DPAC has been provided by national institutions, in particular the institutions participating in the *Gaia* Multilateral Agreement. Observations with the SAO RAS telescopes are supported by the Ministry of Science and Higher Education of the Russian Federation. The renovation of telescope equipment is currently provided within the national project "Science and Universities". The BTA data reduction was performed as part of the SAO RAS government contract approved by the Ministry of Science and Higher Education of the Russian Federation. This work uses data from the Guoshoujing Telescope (the Large Sky Area Multi-Object Fiber Spectroscopic Telescope LAMOST). It is a National Major Scientific Project built by the Chinese Academy of Sciences. Funding for the project has been provided by the National Development and Reform Commission. LAMOST is operated and managed by the National Astronomical Observatories, Chinese Academy of Sciences.

References

Afanasiev, V. L., & Moiseev, A. V. 2005, AstL, 31, 194
Afanasiev, V. L., & Moiseev, A. V. 2011, BaltA, 20, 363
Bahcall, J. N., Kirhakos, S., Saxe, D. H., & Schneider, D. P. 1997, ApJ, 479, 642
Barkhouse, W. A., & Hall, P. B. 2001, AJ, 121, 2843
Banse, K., Ponz, D., Ounnas, C., Grosbol, P., & Warmels R. 1988, igbo.conf, 431
Cardelli, J. A., Clayton, G. C., & Mathis, J. S. 1989, ApJ, 345, 245
Cioni, M.-R. L., Clementini, G., Girardi, L., et al. 2011, A&A, 527, A116
Cioni, M.-R. L., Kamath, D., Rubele, S., et al. 2013, A&A, 549, A29
Chambers, K. C., Magnier, E. A., Metcalfe, N., et al. 2016, arXiv e-prints [arXiv:`1612.05560`]
Chartas, G., Kulkarni, V. P., & Asper, A. 2013, ApJ, 775, 119
Chen, Y.-C., Liu, X., Liao, W.-T., et al. 2020, MNRAS, 499, 2245
Combes, F., Gupta, N., Muller, S., et al. 2021, A&A, 648, A116
Costa, E., Méndez, R. A., Pedreros, M. H., et al. 2011, AJ, 141, 136
Crampton, D., Gussie, G., Cowley, A. P., et al. 1997, AJ, 114, 2353
Dahari, O., & De Robertis, M. M. 1988, ApJS, 67, 249
Dalcanton, J. J., Fouesneau, M., Hogg, D. W., et al. 2015, ApJ, 814, 3
Draine, B. T., & Li 2007, ApJ, 657, 810
Draine, B. T., Aniano, G., Krause, O., et al. 2014, ApJ, 780, 172
de Vaucouleurs, G., de Vaucouleurs, A., Corwin, H. G., et al. 1991, rc3..book
Delchambre, L., Bailer-Jones, C. A. L., Bellas-Velidis, I., et al. 2023, A&A, 674, A31
Dey, A., Najita, J. R., Koposov, S. E., et al. 2023, ApJ, 944, 1
DESI Collaboration (Adame, A. G., et al.) 2024, AJ, 168, 58
Dong, X. Y., Wu, X.-B., Ai, Y. L., et al. 2018, AJ, 155, 189
Dorn-Wallenstein, T., Levesque, E. M., & Ruan, J. J. 2017, ApJ, 850, 86
Fox, A. J., Richter, P., Wakker, B. P., et al. 2013, ApJ, 772, 110
Fox, A. J., Wakker, B. P., Barger, K. A., et al. 2014, ApJ, 787, 147
Flesch, E. W. 2015, PASA, 32, e010
Gaia Collaboration (Vallenari A., et al.) 2023, A&A, 674, A1
Gaia Collaboration (Bailer-Jones, C.A.L., et al.) 2023, A&A, 674, A41
Giveon, U., Maoz, D., Kaspi, S., Netzer, H., & Smith, P. S. 1999, MNRAS, 306, 637
Guo, S., Qi, Z., Liao, S., et al. 2018, A&A, 618, A144
Hamuy, M., Walker, A. R., Suntzeff, N. B., et al. 1992, PASP, 104, 533
Hamuy, M., Suntzeff, N. B., Heathcote, S. R., et al. 1994, PASP, 106, 566
Huo, Z.-Y., Liu, X.-W., Xiang, M.-S., et al. 2013, AJ, 145, 159
Ivanov, V. D., Cioni, M.-R. L., Bekki, K., et al. 2016, A&A, 588, A93
Ivanov, V. D., Cioni, M.-R. L., Dennefeld, M., et al. 2024, A&A, 687, A16
Johnson, L. C., Seth, A. C., Dalcanton, J. J., et al. 2015, ApJ, 802, 127
Jin, J.-J., Wu, X.-B., Fu, Y., et al. 2023, ApJS, 265, 25
Kallivayalil, N., van der Marel, R. P., & Alcock, C. 2006, ApJ, 652, 1213
Kallivayalil, N., van der Marel, R. P., Besla, G., Anderson, J., & Alcock, C. 2013, ApJ, 764, 161
Khan, R. 2017, ApJS, 228, 5
Lang, D. 2014, AJ, 147, 108
Liao, S.-L., Qi, Z.-X., Guo, S.-F., & Cao, Z.-H. 2019, RAA, 19, 029
Luo, A.-L., Zhao, Y.-H., Zhao, G., et al. 2018, yCat, V/153
Lyke, B. W., Higley, A. N., McLane, J. N., et al. 2020, ApJSS, 250, 8
Mainieri, V., Anderson, R. I., Brinchmann, J., et al. 2024, arXiv e-prints [arXiv:`2403.05398`]
Massey, P., Olsen, K. A. G., Hodge, P. W., et al. 2006, AJ, 131, 2478
Massey, P., Neugent, K. F., & Smart, B. M. 2016, AJ, 152, 62
Massey, P., Neugent, K. F., & Levesque, E. M. 2019, AJ, 157, 227
Mateos, S., Alonso-Herrero, A., Carrera, F. J., et al. 2012, MNRAS, 426, 3271
Meusinger, H., Henze, M., Birkle, K., et al. 2010, A&A, 512, A1
Mishra, S., Fox, A. J., Krishnarao, D., et al. 2024, ApJ, 976, L28
Morishita, T. 2021, ApJS, 253, 4
Nedialkov, P., Williams, B. F., Ivanov, V. D., & Valcheva, A. 2018, ATel, 12250
Neugent, K. F., Massey, P., & Georgy, C. 2012, ApJ, 759, 11
Nilson P. 1973, UGC...C, 0
Oke J. B. 1990, AJ, 99, 1621
Peters, C. M., Richards, G. T., Myers, A. D., et al. 2015, ApJ, 811, 95
Peterson, B. M. 1997, iagn.book
Paiano, S., Falomo, R., Franceschini, A., Treves, A., & Scarpa, R. 2017, ApJ, 851, 135
Rao, S. M., Sardane, G., Turnshek, D. A., et al. 2013, MNRAS, 432, 866
Richter, P., Fox, A. J., Wakker, B. P., et al. 2013, ApJ, 772, 111
Rusterucci, S., Martin, N. F., Starkenburg, E., & Ibata, R. 2024, A&A, 692, A30
Sarkisyan, A. N., Vinokurov, A. S., Solovieva, Y. N., et al. 2017, AstBu, 72, 486
Schlafly, E. F., & Finkbeiner, D. P. 2011, ApJ, 737, 103
Schlafly, E. F., Meisner, A. M., & Green, G. M. 2019, ApJS, 240, 30
Skrutskie, M. F., Cutri, R. M., Stiening, R., et al. 2006, AJ, 131, 1163
Storey-Fisher, K., Hogg, D. W., et al. 2024, ApJ, 964, 69
Srianand, R., Gupta, N., Rahmani, H., et al. 2013, MNRAS, 428, 2198
Tody, D. 1986, SPIE, 627, 733
Tody, D. 1993, ASPC, 52, 173
van der Marel, R. P., Fardal, M. A., Sohn, S. T., et al. 2019, ApJ, 872, 24
Vanden Berk, D. E., Richards, G. T., Bauer, A., et al. 2001, AJ, 122, 549
Warmels R. H. 1992, ASPC, 25, 115
Walterbos, R. A. M., & Kennicutt, R. C. 1987, A&AS, 69, 311
Williams, B. F., Hatzidimitriou, D., Green, J., et al. 2014, MNRAS, 443, 2499
Williams, B. F., Lang, D., Dalcanton, J. J., et al. 2014, ApJS, 215, 9
Worseck, G., & Prochaska, J. X. 2011, ApJ, 728, 23
Wright, E. L., Eisenhardt, P. R. M., Mainzer, A. K., et al. 2010, AJ, 140, 1868
York, D. G., Khare, P., Vanden Berk, D., et al. 2006, MNRAS, 367, 945

Appendix A: Observing log

Table A.1: Observing log.

No	*Gaia* EDR3	RA DEC (J2000)	G, mag	Tel.	UT start 20yy-mm-dd Thh:mm	N$_{exp}$× int. time, s	No. in Table B.1	Selection criteria; comments
1*	381231021002898048	00:39:21.921 41:20:31.31	20.52	B	21-11-03T21:18	6×900	15	Opt. colors & PTF variability
2*	381230200663395712	00:39:28.105 41:19:13.09	20.77	B	21-11-03T23:04	4×900	16	Opt. colors & PTF variability
3*	381223637953333376	00:39:34.595 41:07:38.52	19.88	B	21-11-04T19:34	3×900	18	Opt. colors & PTF variability
4*	381251297542795904	00:39:47.423 41:31:47.53	20.31	B	21-10-12T17:17	3×900	21	Opt. colors & PTF variability
5	156600101021498792[a]	00:40:24.514 40:30:25.12	20.00[a]	B	21-12-12T20:37	8×600		Opt. colors & PTF variability; not QSO, X-ray binary?
6*	381129011231416704	00:40:29.727 40:37:05.68	18.98	A	07-11-03T01:34	3×2700	27	X-ray & LGGS
				A	07-11-09T02:07	3×2700		
7	381159003004920192	00:40:45.721 40:51:34.18	19.24	A	20-01-02T04:55	2×1800		*Spitzer* colors & LGGS; too low S/N to interpret
8	381161584267072896	00:41:26.217 40:53:26.55	19.95	A	07-10-10T04:38	3×2700	41	X-ray & LGGS
9	381164710999391104	00:41:37.918 41:01:07.82	19.40	A	07-08-10T08:55	4×1800	45	X-ray & LGGS
10	381276410213544064	00:41:41.408 41:19:16.85	18.57	A	07-10-09T02:05	3×2700	46	X-ray & LGGS
11*	381266244030810880	00:42:15.487 41:20:31.52	20.54	A	10-10-30T02:46	6×2700	57	X-ray & LGGS
12*	369148728241389056	00:42:35.002 40:48:39.20	18.81	A	07-08-11T10:55	3×1200	62	X-ray & LGGS
				A	10-10-30T01:34	3×1500		
13	369257652908605824	00:43:12.746 41:16:25.49	18.58	A	18-10-07T02:27	2×1800		UV excess in LGGS & PHAT; not QSO, star form. region or galaxy?
14	369255522604831232	00:43:53.335 41:16:55.90	19.51	A	07-08-08T07:59	2×1800		X-ray & LGGS; not QSO, early M star
15	369286102772174208	00:44:10.843 41:33:01.15	19.22	A	19-01-08T05:16	2×1500,		*Spitzer* colors & LGGS; flat featureless spectrum
				A		1×602		
16	369281288111420288	00:44:28.716 41:25:45.62	18.96	A	19-01-06T04:03	2×1500,		*Spitzer* colors & LGGS; not QSO, K-type star or glob. cl., at the redshift of M 31
				A		1×1034		
				A	19-01-08T04:17	2×1200		
				A	19-09-05T08:25	3×1500		
				B	22-10-25T17:33	3×900 B		
				B	22-10-25T18:25	2×900 R		
17	369281086247278080	00:44:31.624 41:24:10.69	19.86	A	19-10-27T03:35	6×1800		*Spitzer* colors & LGGS; not QSO, wide emission lines object
18*	369185428738695808	00:44:41.590 40:46:43.46	19.10	B	21-10-02T22:11	3×900 B	79	Opt. colors & PTF variability
				B	21-10-02T22:59	2×900 R		
19	381304653920639488	00:44:45.117 41:47:20.52	19.31	A	19-10-27T01:13	4×1800		*Spitzer* colors + LGGS; too low S/N to interpret
20*	369267681654714112	00:44:48.307 41:16:18.23	18.43	A	19-01-06T01:57	3×900	82	*Spitzer* colors + LGGS
				A	20-01-02T01:57	2×1800		
21*	369189547608980224	00:44:57.601 40:59:13.85	20.47	B	21-12-11T15:20	4×600	83	Opt. colors & PTF variability
22*	369268712447126272	00:44:57.938 41:23:43.72	19.67	A	07-11-09T03:45	2×1800	84	X-ray & LGGS
23	369288714109887744	00:45:27.311 41:32:54.06	20.39	A	18-10-07T08:03	4×1800	92	UV excess in LGGS & *PHAT*
24*	369276756923364224	00:45:28.249 41:29:43.92	19.53	A	18-10-07T05:08	4×1800	93	UV excess in LGGS & PHAT
25	369270469091280000	00:45:43.426 41:20:30.86	19.27	A	07-07-16T08:29	3×1800 B	95	X-ray & LGGS
				A		4×1500 R		
26	375332454650675328	00:46:32.809 42:13:14.25	19.10	A	18-10-07T04:06	3×900		UV excess in LGGS & PHAT; featureless sp., no emission lines
27	375328709439174400	00:46:55.515 42:20:50.09	17.65	A	10-10-30T05:12	3×900	108	X-ray & LGGS
28*	375328395906539392	00:47:02.870 42:18:37.19	19.90	A	10-10-10T07:37	8×836	109	X-ray & LGGS
29*	375328876942905472	00:47:13.476 42:20:47.66	19.92	A	07-07-24T08:05	4×1800	111	X-ray & LGGS
30*	375423881617811328	00:47:39.120 42:26:17.76	18.20	A	19-01-06T02:54	3×1200	115	*Spitzer* colors & LGGS
31	375322314232658048	00:47:42.847 42:10:16.93	19.74	A	08-10-26T01:29	3×2700	116	X-ray & LGGS
32*	375418590218050304	00:47:48.323 42:19:34.31	19.13	A	19-01-08T03:07	3×1200	118	*Spitzer* colors & LGGS
				A	20-01-02T03:10	3×1800		

Notes. The columns indicate (from left to right): target identification, position, *Gaia* G band magnitude, telescope (A – Apache Point 3.5m, B – BTA 6m), UT at the start of the first exposure, number and integration time for the individual exposures (occasionally, the last exposure is shorter because the observations had to be interrupted due to poor weather and there may be a different number of exposures for the blue B and the red R channels), cross-identification with Table B.1, and selection criteria and comments. The astrometry and photometry is from *Gaia* DR3 (Gaia Collaboration 2023a,b), except for object No. 5, marked with “a”, where the data are from Pan-STARRS Survey DR1 (Chambers et al. 2016). The asterisks indicate 16 quasars whose spectra are published for the first time.

Appendix B: Sample of 125 QSOs

Table B.1: Sample of 125 QSOs with redshifts based on optical spectrum, located within M 31 isophote $\mu_B = 26^m/\square''$.

No	*Gaia* DR3 Name	RA DEC J2000	ρ	Gmag, mag	rms, mag	Class	P% QSO	z_{lit}	Ref.	Emis. lines	z_{adopt}	A_V mag	Obs. log ID	Fig. 3 ID
1	380728681624635264	00:36:49.070 +40:08:41.73	1.161	18.921	0.078	uncl	100	0.502±0.051	2		0.502±0.051	0.000±0.134		
2	380803551495086592	00:36:57.656 +40:25:50.28	1.228	19.311	0.095	AGN	97	1.181±0.019	1		1.208±0.005	−0.262±0.076		
								1.181±0.074	2					
								1.208	3					
3	380749950302728832	00:37:35.058 +40:09:41.68	0.997	18.682	0.114	AGN	100	0.337±0.001	1		0.337±0.085	0.040±0.129		
								0.337±0.085	2					
								0.335	4					
4	380736962321466240	00:37:50.796 +40:04:17.14	0.969	20.474	0.149	AGN	38	1.546±0.018	1		1.264±0.430	0.057±0.223		
								1.264±0.430	2					
...	....	....	.....	.....	.....	....	....	.....	...	....	.....	......	.....	....
55	369145670224353664	00:42:14.124 +40:39:20.52	0.683	18.770	0.147	AGN	90	0.775±0.007	1		0.7579±0.0007	0.396±0.110		
								0.775±0.354	2					
								0.757	8					
								0.7579±0.0007	6;8	MgII 2799, OII 3727, $H\beta$ 4863, OIII 4959 & 5007				4214.1+4039L
56	369145773303561856	00:42:14.991 +40:39:09.54	0.690	19.874	0.113	AGN	46	1.780±0.010	1		1.778±0.001	0.079±0.034		
								1.774	9					
								1.778±0.001	6;9	CIV 1548, CIII] 1909				4214+4039M
57	381266244030810880	00:42:15.487 +41:20:31.52	0.249	20.549	0.156	NA	-	1.520±0.020	6	CIV 1548, CIII] 1909, MgII 2799	1.520±0.020	0.259±0.400	11	4215+4120A
...	....	....	.....	.....	.....	....	....	.....	...	....	.....	......	.....	....

Notes. The position and the ID are from *Gaia* DR3 (Gaia Collaboration 2023a), except for the objects marked with ^{a}, whose information comes from Pan-STARRS Survey DR1 (Chambers et al. 2016). The distance ρ within the rectified plane of M 31 is in fractions of the major isophotal radius ρ_{25}. The Class (name of best class) and the probability of the object being a quasar P_{QSO} (in %) from the Discrete Source Classifier-Combmode from *Gaia* DR3 (Gaia Collaboration 2023b); when an object is missing a Class, we list its Class as inclassified, "uncl", and if the object has no entry, then the Class is set to not applicable, "NA". References: (1) Gaia Collaboration (2023a); (2) Storey-Fisher et al. (2024); (3) Dey et al. (2023); (4) Huo et al. (2013); (5) Neugent et al. (2012); (6) this work; (7) Dong et al. (2018); (8) Liao et al. (2019); (9) Massey et al. (2019); (10) Dahari & De Robertis (1988); (11) Meusinger et al. (2010); (12) Dorn-Wallenstein, Levesque, & Ruan (2017); (13) Nedialkov et al. (2018); (14) Rao et al. (2013); (15) Paiano et al. (2017). Multiple references are given when we have reanalyzed spectra from the literature to remeasure the redshifts. Finally adopted redshift z_{adopt} is explained in Sect. 4.3. The analyzed original spectra are suffixed by A (Apache Point) or B (BTA) in the last column, while the reanalyzed literature spectra are suffixed by M (Mayall) or L (LAMOST). Here we show only an example subset of the table, for guidance. The entire table is only available in electronic form at the CDS via anonymous ftp to cdsarc.u-strasbg.fr (130.79.128.5) or via http://cdsweb.u-strasbg.fr/cgi-bin/qcat?J/A+A/.

Appendix C: Data availability

Table C.1 lists the spectra of J004029.727+403705.68 and J004215.487+412031.52 that are reported for the first time in this paper.

Table C.1: New spectra of J004029.727+403705.68 (id. 1) and J004215.487+412031.52 (id. 2), reported here for the first time.

λ [Å]	Flux [arbitrary units]	Index
3533	1.1040	1
3535	1.2220	1
3537	0.9950	1
3538	1.2290	1
3540	1.0410	1
3542	0.9604	1
3544	1.2930	1
	...	
3801	0.4288	2
3803	1.1960	2
3805	1.2750	2
3807	1.7420	2
3809	0.7665	2
3811	1.5950	2
3813	2.0270	2
	...	

Notes. Only part of the table is shown as an example. The entire table is only available in electronic form at the CDS via anonymous ftp to cdsarc.u-strasbg.fr (130.79.128.5) or via http://cdsweb.u-strasbg.fr/cgi-bin/qcat?J/A+A/.

Appendix D: Intrinsic colors of quasars

Table D.1 lists the derived intrinsic colors of quasars, as shown with black lines in Fig. 5.

Table D.1: Intrinsic colors of quasars.

z	$(g-r)$ [mag]	$(g-i)$ [mag]	$(g-z)$ [mag]	$(g-y)$ [mag]	N
0.1	0.222±0.151	0.569±0.258	0.586±0.239	0.697±0.286	8
0.3	0.266±0.201	0.408±0.305	0.800±0.264	0.612±0.402	79
0.5	0.062±0.168	0.312±0.258	0.297±0.321	0.694±0.272	138
0.7	0.061±0.120	0.138±0.213	0.254±0.224	0.251±0.298	187
0.9	0.118±0.163	0.118±0.235	0.190±0.251	0.306±0.294	249
1.1	0.250±0.118	0.229±0.173	0.159±0.193	0.319±0.223	273
1.3	0.262±0.124	0.287±0.182	0.257±0.193	0.314±0.197	270
1.5	0.193±0.130	0.349±0.160	0.327±0.167	0.339±0.216	295
1.7	0.081±0.116	0.301±0.174	0.286±0.160	0.329±0.210	262
1.9	0.078±0.119	0.260±0.148	0.337±0.174	0.392±0.196	222
2.1	0.092±0.111	0.178±0.162	0.357±0.179	0.367±0.197	173
2.3	0.076±0.116	0.151±0.145	0.325±0.177	0.442±0.171	174
2.5	0.080±0.121	0.123±0.162	0.235±0.157	0.440±0.164	124
2.7	0.136±0.134	0.213±0.178	0.280±0.161	0.434±0.223	94
2.9	0.119±0.119	0.225±0.163	0.204±0.165	0.377±0.131	62
3.1	0.248±0.085	0.361±0.223	0.306±0.201	0.467±0.160	34

Notes. N is the number of quasars in the respective redshift z bin (bin size 0.2 dex); the numbers of some colors can be smaller if there are quasars with missing photometry.

Appendix E: Correction of the *Spitzer* coordinates

The coordinate accuracy of candidate quasars is crucial for their cross-identification for the optical spectroscopic follow-up. Most of our candidates are selected on the base of their *Spitzer* photometry (Khan 2017), but a comparison with various near-infrared and optical catalogs revealed systematic offsets in this coordinate system. Therefore, we decided to transfer the *Spitzer* coordinates of Khan (2017) to the WISE J2000 coordinate system. We cross-matched the *Spitzer* and WISE coordinates with $3''$ matching radius, for objects with $[W2]\leq13.5$ mag and -0.35 mag$\leq[W2]-[W1]\leq0.35$ mag as shown in Fig. 2 (top right panel), to ensure we only consider high signal-to-noise detections and to reduce the number of spurious matches. Then, we formed the *Spitzer*–WISE

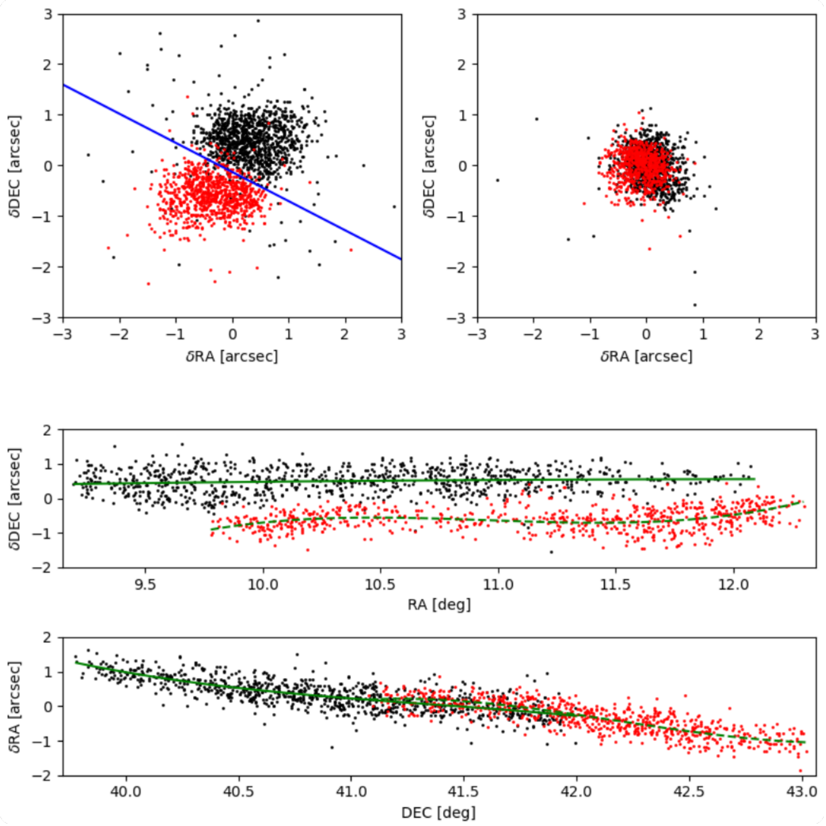

Fig. E.1: Upper left: δRA/δDEC plot for the astrometric *Spitzer*–WISE comparison of 1623 objects from our bright astrometric sample. The double central clump is due to small systematic deviations in the Khan (2017) coordinate system. The blue line makes initial division of the astrometric sample into two spatially distinct subsamples of ~700 and ~900 objects (see Fig. E.2). Upper right: Same plot after 3σ clipping and correcting for the systematic effect to the WISE coordinate system. Middle: δDEC(*Spitzer*–WISE) vs. WISE RA. Bottom: δRA(*Spitzer*–WISE) vs. WISE DEC. The solid and dashed green curves are the best fits to the trends for the two subsamples in the middle and bottom panels (see text).

coordinate differences δRA and δDEC, for these sources, plotted them versus each other (Fig. E.1, top left) and saw a two-clump structure. We imposed an initial separation between the two clumps along the blue line. The objects above and below it (plotted everywhere with black and red dots, respectively) are located into two distinct spatial regions on the sky, separated with a line connecting the following positions in RA, DEC (J2000), in degrees: (9.714, 41.195), (10.140, 41.048), (10.963, 41.874), (11.685, 41.874), (11.920, 42.010) and (12.186, 42.005) – marked with green solid line in Fig. E.2. For all objects within each of these two areas we separately derived polynomial fits, with 3σ clipping, of δRA and δDEC versus DEC and RA, respectively (Fig. E.1, middle and lower panels), based on about 1600 objects in total:

$$\delta DEC_{black} = -1.671 + 0.36211 \times RA - 0.014715 \times RA^2, \tag{E.1}$$

$$\delta DEC_{red} = -405.401 + 107.03023 \times RA - 9.006573 \times RA^2 + 0.2022619 \times RA^3 + 0.00327904 \times RA^4, \tag{E.2}$$

$$\delta RA_{black} = -26974.840 + 1920.434447 \times DEC - 45.5512001 \times DEC^2 + 0.35995935 \times DEC^3, \tag{E.3}$$

$$\delta RA_{red} = 8571.288 - 620.935448 \times DEC + 15.0056471 \times DEC^2 - 0.12096752 \times DEC^3. \tag{E.4}$$

The typical RMS of these relations is ~0.3″. Applying them brings the two clumps together (Fig. E.1, upper right panel).

A minor caveat in this correction is the omission of the proper motions of the brightest sources that are probably Milky Way stars, but the *Gaia* DR3 suggests there are of order of 10-20 mas yr^{-1}. Fortuitously, the *Spitzer*–WISE time baseline is ~ 5 yr , so any cumulative effect from the proper motions can safely be neglected.

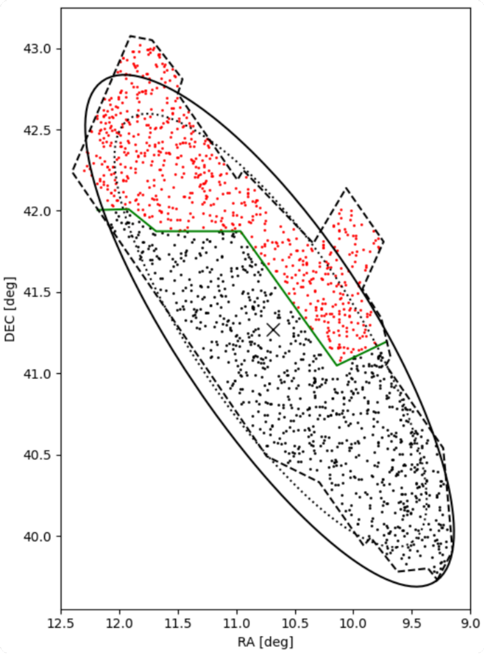

Fig. E.2: Map of our astrometric sample of 1623 objects with the adopted final dividing solid line (solid green) for the two spatially distinct samples of 710 (red dots) and 913 (black dots) objects. The dashed line shows the approximate outline of the Khan (2017) catalog; the solid and dotted lines show the $\mu_B = 26^m/\square''$ and μ_B=$25^m/\square''$ isophotes, respectively. M 31 center is marked with an x.